nature materials

ARTICLES

https://doi.org/10.1038/s41563-019-0542-x

Synthesis of orthogonally assembled 3D cross-stacked metal oxide semiconducting nanowires

Yuan Ren[1,5], Yidong Zou[1,5], Yang Liu[2], Xinran Zhou[1], Junhao Ma[1], Dongyuan Zhao[1], Guangfeng Wei[3], Yuejie Ai[2], Shibo Xi[4] and Yonghui Deng[1*]

Assemblies of metal oxide nanowires in 3D stacks can enable the realization of nanodevices with tailored conductivity, porous structure and a high surface area. Current fabrication methods require complicated multistep procedures that involve the initial preparation of nanowires followed by manual assembly or transfer printing, and thus lack synthesis flexibility and controllability. Here we report a general synthetic orthogonal assembly approach to controllably construct 3D multilayer-crossed metal oxide nanowire arrays. Taking tungsten oxide semiconducting nanowires as an example, we show the spontaneous orthogonal packing of composite nanorods of poly(ethylene oxide)-block-polystyrene and silicotungstic acid; the following calcination gives rise to 3D cross-stacked nanowire arrays of Si-doped metastable ε-phase WO_3. This nanowire stack framework was also tested as a gas detector for the selective sensing of acetone. By using other polyoxometallates, this fabrication method for woodpile-like 3D nanostructures can also be generalized to different doped metal oxide nanowires, which provides a way to manipulate their physical properties for various applications.

Nature is abundant with fascinating materials, such as natural diatomite, shell and nacre. They are constructed via self-assembly with ordinary building units into multifunctional nanostructures and can exhibit superior physiochemical properties[1]. Recently, self-assembly nanomaterials based on organic–inorganic assembled nanostructures, such as biological mineralization and bionic materials, have resulted in extensive and interdisciplinary applications as sensor devices, drug delivery vehicles and energy storage and electrochromic devices[2,3]. The self-assembly strategy has emerged as a flexible and powerful approach to design various functional nanostructures via the spontaneous organization of host molecules and inorganic and/or organic guests through non-covalent interactions, which include hydrogen bonding, π–π stacking, hydrophilic–hydrophobic interactions and even electrostatic interactions[4,5]. Among various nanostructures, nanowire-based structures, particularly semiconducting nanowires, have attracted particular attention because of their excellent properties, such as direct electron transport and good mechanical stability[6,7]. Traditional techniques require special equipment and multistep procedures, which include the preparation of nanowires and further manual assembly or costly transfer printing, and thus lack fabrication flexibility[8–10]. The efficient and convenient synthesis of nanowire-based structures with highly controllable morphology, size and functionalities still remains a major challenge[11–14].

Block copolymers (BCPs) exhibit rich phase separation behaviours and can self-assemble into various nanostructures[15]. Based on their flexible soft chemistry behaviour, BCPs have been employed as structure-directing agents to construct organic or inorganic nanowire patterns[16–21]. These inorganic structures usually consist of inorganic nanowires faithfully derived from the self-assembled structure of the BCPs via either conversion of the silicon-containing segments or post-decoration of the assembled nanostructures with inorganic precursors. Within these structures, the interfaces between the wires are distinct, and multiple components can be integrated in each layer for applications other than those of the single component-based structures.

The co-assembly of amphiphilic copolymers and inorganic precursors was developed to be a more effective approach for various ordered nanostructures by virtue of the tunable and reproducible interfacial interactions between the amphiphilic structure-directing molecules and inorganic precursors[22–26]. However, little work has been done yet to controllably construct metal oxide semiconductor nanowire arrays through the cooperative assembly of organic amphiphilic copolymers and inorganic precursors that are suitable for the reliable, and flexible mass production of nanowire-based nanostructures and nanodevices for various applications[27–29].

Here we successfully explored an unusual BCP-directed orthogonal assembly to conveniently construct 3D multilayer-crossed metal oxide semiconducting nanowire arrays through the co-assembly of amphiphilic diblock copolymers and polyoxometallates (POMs) and the subsequent calcination-induced structure transformation. Taking the fabrication of 3D tungsten oxide nanowire arrays as an example (Fig. 1 and Supplementary Fig. 1), poly(ethylene oxide)-block-polystyrene (PEO-b-PS) and hydrated silicotungstic acid ($H_4SiW_{12}O_{40}$•$15H_2O$, abbreviated as H_4SiW) can co-assemble to form multilayer-crossed tungsten oxide nanowire arrays (MC-WO_3-NWAs). Interestingly, the obtained tungsten oxide nanowires were found to have a unique metastable ε-WO_3 phase due to the introduction of silicon atoms in situ generated by H_4SiW. The obtained semiconducting MC-WO_3-NWAs were used as acetone sensors and showed sensitivity down to 10.0 ppb, fast response-recovery dynamics and good selectivity due to the simultaneous effect of high surface areas with numerous active sites for gas–solid catalytic

[1]Department of Chemistry, Shanghai Key Laboratory of Molecular Catalysis and Innovative Materials, State Key Laboratory of Molecular Engineering of Polymers, and iChEM, Fudan University, Shanghai, China. [2]College of Environmental Science and Engineering, North China Electric Power University, Beijing, China. [3]School of Chemical Science and Engineering, Shanghai Key Laboratory of Chemical Assessment and Sustainability, Tongji University, Shanghai, China. [4]Institute of Chemical and Engineering Sciences, Agency for Science, Technology and Research in Singapore (A*STAR), Jurong Island, Singapore. [5]These authors contributed equally: Yuan Ren, Yidong Zou. *e-mail: yhdeng@fudan.edu.cn

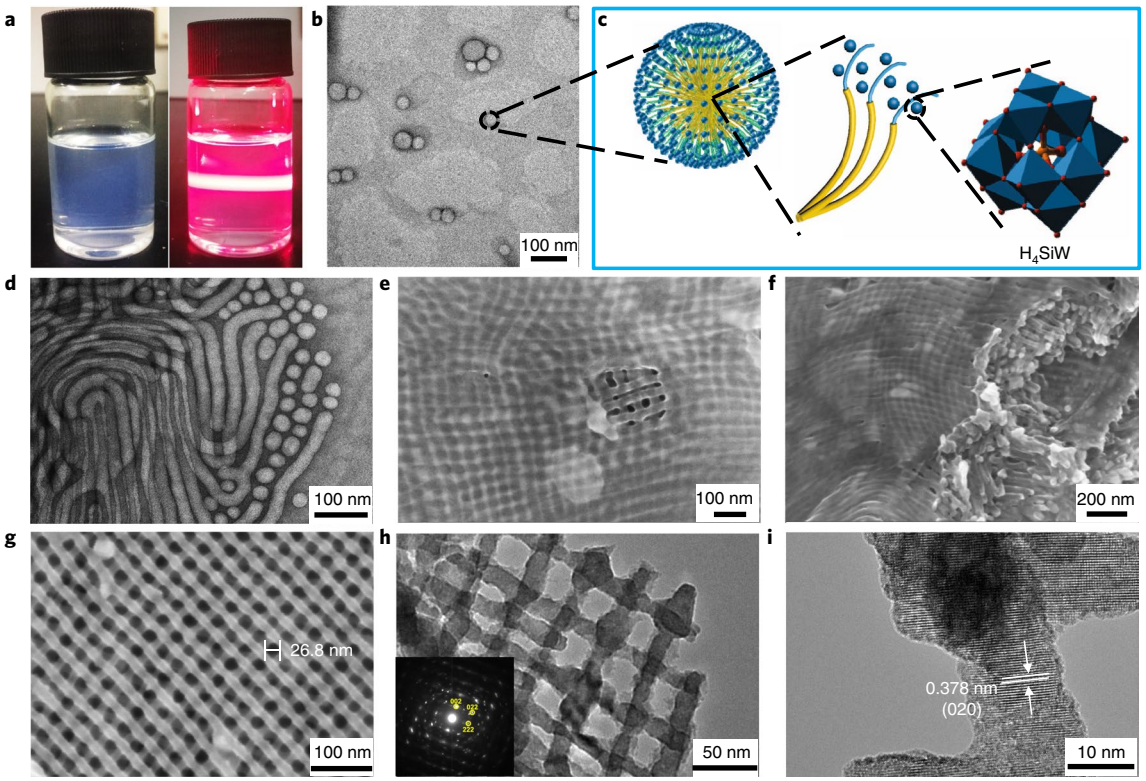

Fig. 1 | Co-assembly of PEO-b-PS and $H_4SiW_{12}O_{40}$. **a**, Optical photographs of the transparent colloidal PEO-b-PS/H_4SiW/THF solution showing a pale blue due to the light scattering of the micelle solution (left) and corresponding Tyndall effect under a 650 nm red laser illumination (right). **b**, Cryo-TEM image of the colloidal micelles. **c**, Structural models of composite micelles. Yellow line, PS block; blue line, PEO block; red dot, O atom; blue polyhedron, W–O octahedron; orange dot, Si atom). **d**, TEM image of the spherical and cylindrical micelles. **e**,**f**, Field-emission scanning electron microscopy (FESEM) images of the as-cast PEO-b-PS/H_4SiW hybrid film composed of multilayer-crossed cylindrical micelles. **g**–**i**, FESEM (**g**) and TEM (**h** and **i**) images with a selected-area electron diffraction pattern (**h**) of MC-WO_3-NWAs obtained after calcination.

reactions, the high electron transport along the nanowires and the high electric dipole moment of ε-WO_3.

Remarkably, this BCP-directed co-assembly method can be extended readily to synthesize various multilayer-crossed metal oxide nanowires with different compositions. We have demonstrated the 3D cross-stacked nanowire structures of Si-doped MoO_3, P-doped WO_3 and P-doped MoO_3 by using $H_4SiMo_{12}O_{40}$, $H_3PW_{12}O_{40}$ and $H_3PMo_{12}O_{40}$, respectively, which have promising applications in catalysis, sensing, energy storage and conversion, and so on.

Interfacial behaviour of micelles

Through mixing the two homogeneous colourless tetrahydrofuran (THF) solutions, one that contained dissolved PEO-b-PS copolymers and the H_4SiW, a stable, transparent and pale blue colloidal solution with a solid (copolymer and H_4SiW) content of 0.08 g ml^{-1} (Supplementary Fig. 2), which exhibits a typical Tyndall effect (Fig. 1a). The formation of such a colloidal solution can be explained as follows. The PEO segments of PEO-b-PS can be quickly protonated by H^+ ions released from H_4SiW that further interact with $SiW_{12}O_{40}^{4-}$ anions by electrostatic attractions[30,31], which significantly increases the repulsion force among the copolymers and induces their spontaneous micellization to reduce interface energy. Thus, uniform spherical micelles with a THF-swelled PS core and H_4SiW-associated PEO shell formed, as confirmed by cryo-transmission electron microscopy (TEM) (Fig. 1b). Dynamic light scattering measurements show bimodal narrow size distributions (Supplementary Fig. 3). The first distribution peak, centred at 28.5 nm, corresponds to PEO-b-PS/H_4SiW spherical micelles, and the other peak at 2.5 nm is attributed to free $SiW_{12}O_{40}^{4-}$ anions. Given that the molecule size of $SiW_{12}O_{40}^{4-}$ is about 1.5 nm (ref. [32]), the THF-solvation shell thickness around $SiW_{12}O_{40}^{4-}$ is about 0.5 nm. Strikingly, when the colloidal solution was dropped directly onto carbon-coated copper grids for normal TEM characterization, numerous cylindrical micelles and some spherical micelles could be observed (Fig. 1d). The nanospheres have the same size as that in the cryo-TEM image, whereas the cylindrical micelles have different lengths that range from 50 nm to several micrometres, but the same diameter of about 25 nm (Fig. 1d and Supplementary Fig. 4). Moreover, the cylindrical micelles exhibit a bumpy morphology with close spherical tips, which suggests that most of the spherical micelles gradually fused into cylindrical micelles in line with the THF evaporation (Supplementary Fig. 4d). When the whole colloidal solution was cast on Petri dishes, an organic–inorganic composite film that consists of multilayer-crossed cylindrical micelles can be obtained due to the slow assembly of micelles under a higher concentration with sufficient building blocks (Fig. 1e,f and Supplementary Fig. 5).

Structural transformation induced by calcination

The as-formed H_4SiW/PEO-b-PS film was calcined at 500 °C in nitrogen and then at 400 °C in air, which resulted in an unusual kind of 3D MC-WO_3-NWAs (Fig. 1g). The nanowires are ordered in one direction within each layer but crossed between adjacent layers, and most of the cross-angles are close to 90° (Supplementary Fig. 6). The spacing between two neighbouring nanowires is ~20.0 nm, and the diameter of the WO_3 nanowires is ~15.0 nm. By increasing the mass ratio of H_4SiW/PEO-b-PS from 2.0 to 3.0, 4.0 and 5.0, similar nanostructures of nanowire arrays can be obtained, except that the diameter of the nanowires increases from ~10.5 to ~18.5 nm because

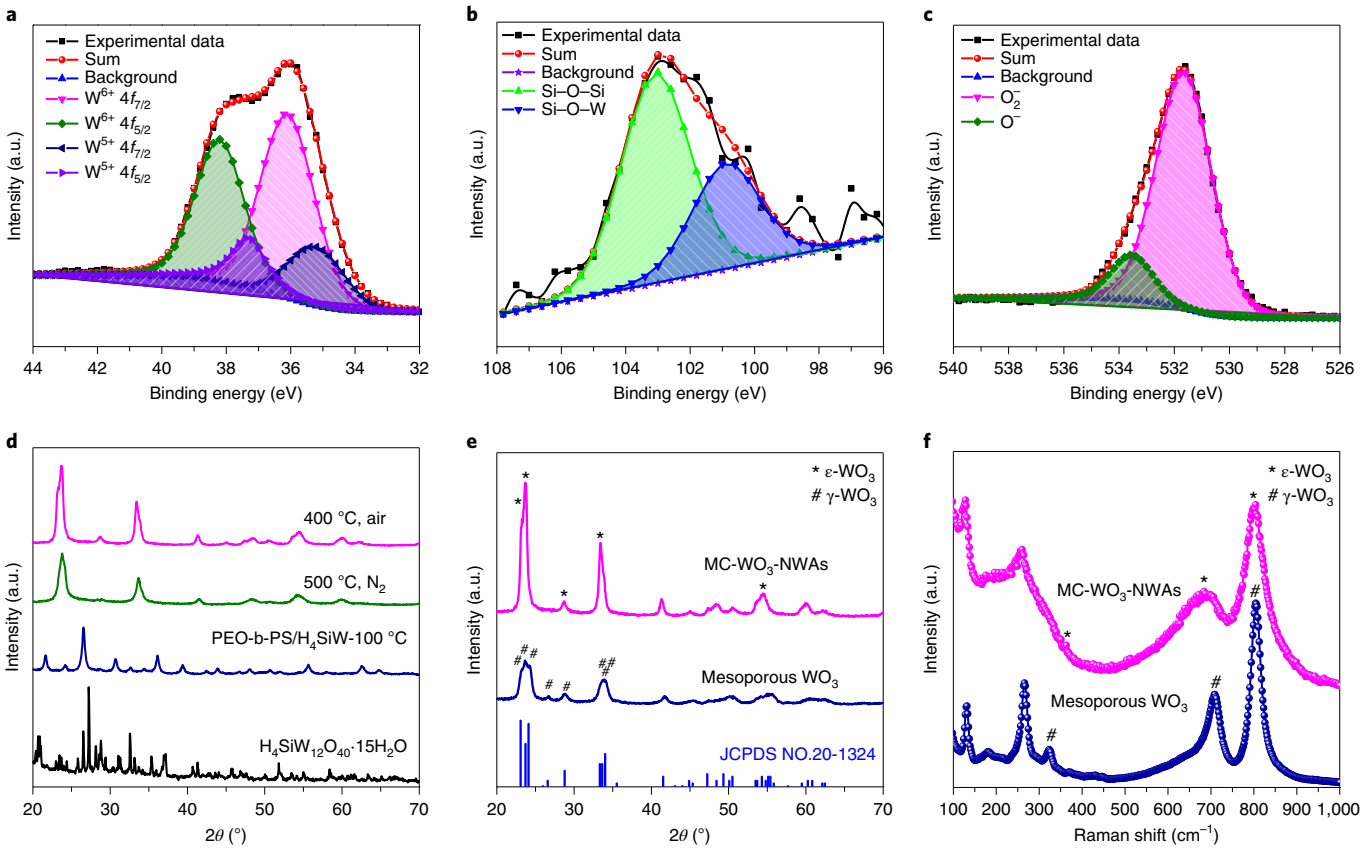

Fig. 2 | Elemental and structural analysis of the MC-WO_3-NWAs. a–c, X-ray photoelectron spectroscopy showing the W 4*f* (**a**), O 1*s* (**b**) and Si 2*p* (**c**) core level peak regions of MC-WO_3-NWAs. **d**, XRD patterns of completely Si-doped ε-WO_3 after thermal treatment at 500 °C in N_2. After calcination in air at 400 °C to remove the residual carbon derived from the organic templates, the Si-doped ε-WO_3 materials had crystalline features. **e**,**f**, XRD patterns (**e**) and Raman spectra (**f**) of MC-WO_3-NWAs and the mesoporous WO_3 (the control sample) obtained using WCl_6 as the inorganic precursor. The MC-WO_3-NWAs sample displays peaks at 363, 682 and 804 cm^{-1}, which correspond to the acentric ε-phase (space group *Pc*). In contrast, mesoporous WO_3 displays peaks at 324, 710 and 805 cm^{-1}, assigned to the γ-WO_3 phase (space group *P*21/*n*). a.u., arbitrary units.

more H_4SiW species are involved in interacting with the ethylene oxide segments of PEO-b-PS copolymers (Supplementary Fig. 7). Excess addition of H_4SiW can result in degenerated MC-WO_3-NWAs that consist of non-uniform and even broken nanowires. TEM images (Fig. 1h,i) show a clearly porous structure formed by the interweaving crystalline semiconducting WO_3 nanowires, and the nanowires are 'welded' at the crossing points. The selected-area electron diffraction pattern reveals spotty diffraction arrays, in which the diffraction spots are slightly elongated. A close observation on a single nanowire reveals the presence of a distorted crystal lattice and some dislocations (Supplementary Fig. 8a,b) or lattice mismatches at crystal grain boundaries (Supplementary Fig. 8c,d). Therefore, the nanowires in the MC-WO_3-NWAs are not perfect single crystals. The pore structure was evaluated by nitrogen adsorption–desorption isotherms, which indicate a mean pore size of about 29.0 nm and specific surface area of 55 $m^2 g^{-1}$ (Supplementary Fig. 9 and Supplementary Note 1).

The unique structural transformation from cylindrical composite micelles into nanowires induced by calcination can occur even if the concentration of the PEO-b-PS/H_4SiW solution changes (Supplementary Figs. 10–13 and Supplementary Note 2). In situ TEM was employed to further study the formation by heating the as-casted PEO-b-PS/H_4SiW under TEM and by real-time recording images of the sample (Supplementary Video 1). The well-aligned cylindrical micelles can be maintained up to 300 °C during TEM observation, and are quickly transformed into nanowire arrays at 340 °C, due to the accelerating effect under vacuum that promotes the decomposition of the composite[33–35]. X-ray photoelectron spectroscopy characterization of the MC-WO_3-NWAs reveals the core level peaks of W 4*f*, O 1*s* and Si 2*p* (Fig. 2a–c and Supplementary Fig. 14), which confirms the presence of W and Si and species. The peak-differentiation-imitating analysis indicates the presence of small amount of W^{5+} (24.3%), and the O 1*s* peak also reveals the oxygen vacancy in the WO_3 crystal lattice of MC-WO_3-NWAs. Energy dispersive spectra show the uniform distribution of W, O and Si throughout the MC-WO_3-NWAs sample[36] (Supplementary Fig. 15).

The obtained MC-WO_3-NWAs show well-resolved X-ray diffraction (XRD) peaks attributed to the unusual ε-WO_3 crystallites (JCPDS No. 20-1324) (Fig. 2d,e). Compounds with the ε-phase WO_3 have been extensively studied as ferroelectric materials for their spontaneous polarization behaviour and this phase usually exists only at a low temperature (<350 °C) (refs [37–39]). Following a similar solvent-evaporation-induced co-assembly, WCl_6 was used as the tungsten source to assemble with PEO-b-PS via the complexation between the PEO segments and the tungsten species[40], and an ordered mesoporous WO_3 was obtained via sol–gel chemistry (Supplementary Fig. 16). The obtained mesoporous WO_3 has 3D interconnected spherical mesopores and the polycrystalline γ-phase WO_3. Such a dramatic difference in crystal phase is also evidenced by the Raman spectroscopy measurements (Fig. 2f). These results clearly indicate that the silicon-containing

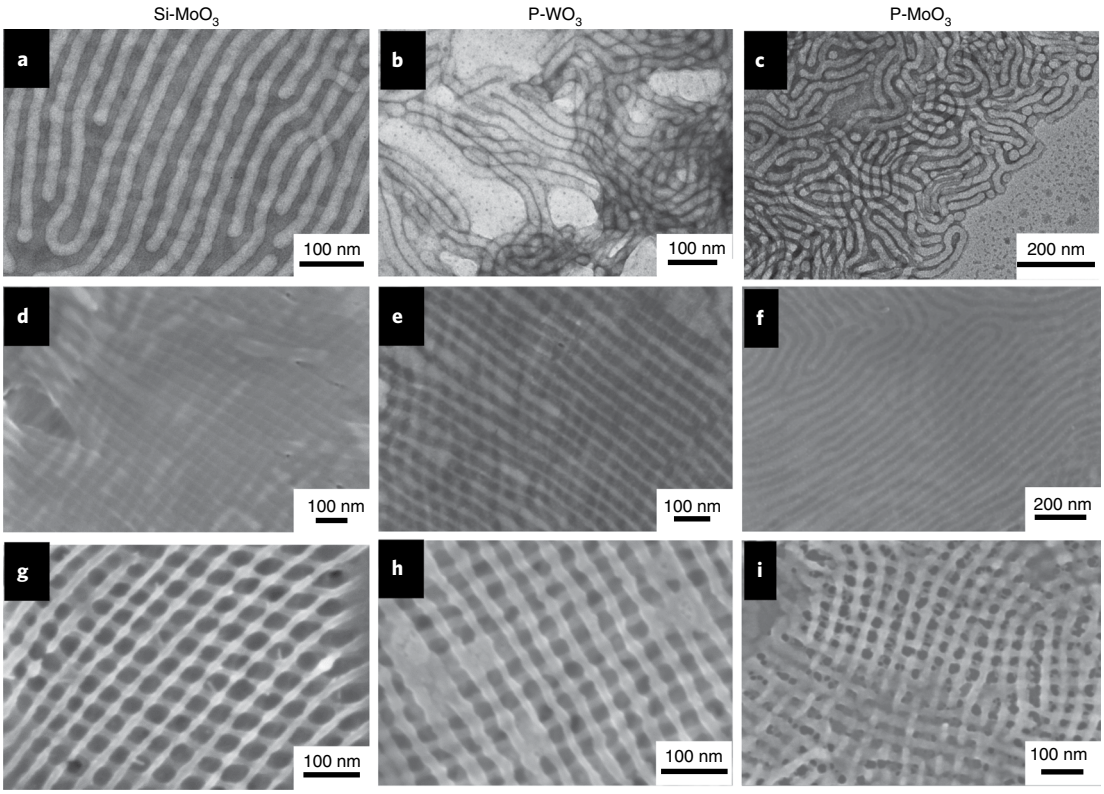

Fig. 3 | Different 3D cross-stacked nanowire structures by using other POMs as inorganic precursors. a–c, TEM images of as-cast PEO-b-PS/POM cylindrical micelles of $SiMO_3$ (**a**), PWO_3 (**b**) and $PMoO_3$ (**c**). **d–i**, FESEM images of hybrid films before (**d–f**) and after (**g–i**) calcination. The corresponding MC-metal oxide-NWAs were obtained using silicomolybdic acid (**a**, **d** and g), phosphotungstic acid (**b**, **e** and **h**) and phosphomolybdic acid (**c**, **f** and **i**) as the inorganic precursors.

species play an important role in stabilizing the metastable ε-WO_3, especially when they are used at temperatures higher than 350 °C. The one-step in situ Si-doping strategy using a Si-containing tungsten precursor shows great advantages in synthesizing ε-WO_3 materials, with controllable nanostructures and compositions (Supplementary Note 3).

It is noteworthy that, following a similar process, other Keggin-type POMs, such as $H_4SiMo_{12}O_{40}$, $H_3PW_{12}O_{40}$ and $H_3PMo_{12}O_{40}$, can be employed to co-assemble with PEO-b-PS copolymers to controllably synthesize Si-doped MoO_3, P-doped WO_3 and P-doped MoO_3 NWAs, respectively (Fig. 3). The co-assembly, structural transformation and the morphology and structure of the obtained P-doped materials are similar to those of MC-WO_3-NWAs, as confirmed by various characterization techniques, which include electron microscopy and element mapping (Supplementary Table 1), XRD (Supplementary Fig. 17), thermogravimetric analysis (Supplementary Fig. 18) and X-ray photoelectron spectroscopy (Supplementary Figs. 19–21). Moreover, binary hybrid nanowire arrays can also be obtained through similar methods, and other BCPs with features similar to those of PEO-b-PS can be used for such syntheses (Supplementary Figs. 22–28 and Supplementary Note 3)[40].

Synthesis mechanism

Based on the above results, it was speculated that the formation of the 3D interlaced metal oxide nanowires (for example, MC-WO_3-NWAs) experiences three stages, (1) the co-assembly of PEO-b-PS and silicotungstic acid into spherical composite micelles, (2) the fusion of the spherical micelles into cylindrical micelles that subsequently self-assemble into a multilayer-crossed nanostructure and (3) the thermal-treatment-induced structural transformation into MC-WO_3-NWAs, as vividly illustrated in Fig. 4a and the animation (Supplementary Video 2, Supplementary Figs. 29 and 30 and Supplementary Note 4). In the second stage, the cylindrical micelles with a high aspect ratio in the solution usually tend to self-assemble into a 2D hexagonal structure (*P6mm*) to reach a closest packing as the solvent evaporation proceeds[41,42]. The distance between the neighbouring two layers is $\sqrt{3}r$, where r is the radius of the micelles (Fig. 4b, right). However, the PEO-b-PS/H_4SiW cylindrical micelles were closely stacked parallel within every layer, and nearly orthogonally between adjacent layers. In this case, the interlamellar spacing increases to $2r$ (bottom of Fig. 4b), which favours formation of a stable stacked structure due to the weaker electrostatic repulsion between the cylindrical micelles.

To illustrate the formation mechanism for the orthogonally assembled structure, a simplified simulation was carried out. As mentioned in the above dynamic light scattering results, the diameter of the cylindrical micelles is about 25 nm, and the thickness of the THF solvated region around a single $H_4SiW_{12}O_{40}$ is about 0.5 nm. These cylindrical micelles further precipitate and co-assemble at the solid (silicon substrate)–liquid (precursor solution)–gas (air) interface where a meniscus exists (Fig. 4a). This allows for a rapid evaporation of solvent, which induces the cylindrical micelles to assemble parallel and orthogonally such that neighbouring layers minimize the repulsion force among them. The dynamic distance between the neighbouring cylindrical micelles within the same layer is 1.0 nm, which corresponds to twice the thickness of the THF-solvated region. Based on these considerations, the electrostatic repulsive force (defined as $F=q^2/4\pi\varepsilon r^2$, where q is the quantity of electric charge of the micelles and ε is the dielectric constant of the solution) between a single free cylindrical micelle and the preformed arrays of cylindrical micelles varies as the crossing angle changes from 0 to 180° (top of Fig. 4c). The electrostatic repulsive force (F) reaches

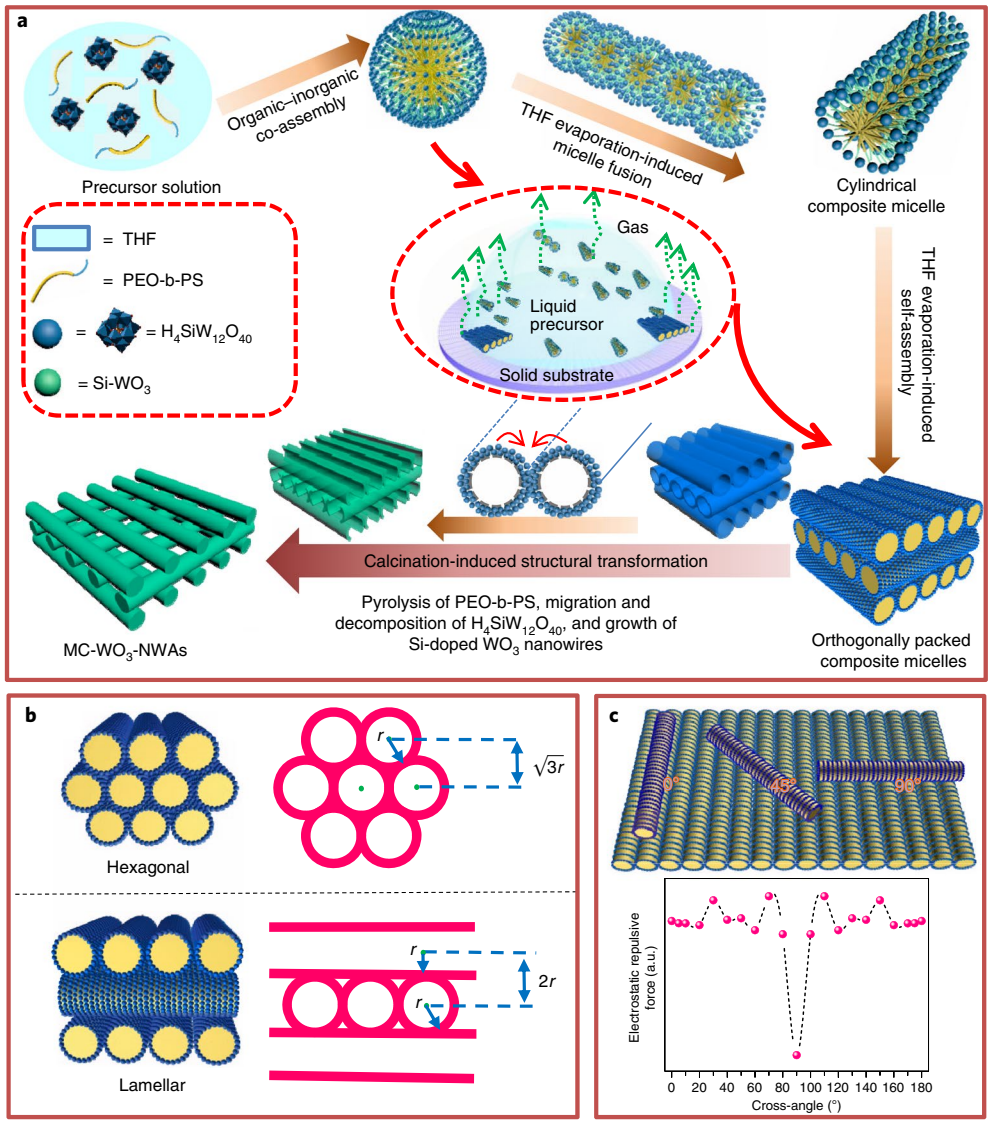

Fig. 4 | Schematic illustration and theoretical simulation of the formation process of the MC-WO_3-NWAs. a, First, PEO-b-PS and $H_4SiW_{12}O_{40}$ in a THF solution co-assemble into the spherical composite micelles. Second, solvent evaporation induces the fusion of the composite spherical micelles into cylindrical micelles that subsequently self-assemble into a multilayer-crossed nanostructure. Finally, the removal of the organic templates and the transformation of $H_4SiW_{12}O_{40}$ in the organic–inorganic composites into Si-doped WO_3 nanowires. The inset in the centre of the scheme depicts the assembly of cylindrical composite micelles into orthogonally packed arrays at the solid–liquid–gas interface with the continuous evaporation of THF. **b**, Comparison of the hexagonal and lamellar structure constructed by PEO-b-PS/H_4SiW cylindrical composite micelles. **c**, A stacking model of the negatively charged PEO-b-PS/H_4SiW cylindrical micelles (top) and simulation results of the electrostatic repulsive force between a single free cylindrical micelle and the preformed arrays of cylindrical micelles as the cross-angle changes from 0 to 180° bottom).

its minimum at 90° (bottom of Fig. 4c and Supplementary Table 2). Clearly, the cylindrical micelles between the layers prefer to cross vertically to reach the most stable structure, and the theoretical simulation results agree well with the scanning electron microscopy and TEM characterizations.

DFT calculations and EXAFS analyses

To understand the contribution of Si in stabilizing the unusual metastable ε-WO_3 phase of MC-WO_3-NWAs, synchrotron-radiation-based X-ray absorption fine structure (XAFS) spectroscopy and density functional theory (DFT) were applied to directly resolve the crystal structure and atomic energy of MC-WO_3-NWAs. It was found that the change of formation energy caused by Si doping followed the order of Si^{4+} embedded (Type I, 23.53 eV, Fig. 5a) > 0 eV > Si^{4+} embedded (Type II, −10.36 eV, Supplementary Fig. 31b) > W^{6+} substituted (−171.55 eV, Supplementary Fig. 31c). This indicates that Si^{4+} embedded in the crystal lattice of γ-WO_3 is an optimal and stable doping type, which can induce partial lattice distortion and lead to the ε-WO_3 phase. In addition, the isosurface of the electron density difference for Si-doped WO_3 represents rigorously vertical transitions, and is most amenable to depict optically populated Franck–Condon states (Fig. 5b), and a partial charge transfer occurred from W^{6+} to Si^{4+} to form stable Si–O–W bonds. The density of states (DOS) for pure WO_3 and Si-doped WO_3 indicate that the calculated bandgap of Si-doped WO_3 (0.99 eV) is lower than that for pure WO_3 (1.29 eV). This implies that the introduction of Si^{4+} can reduce the bandgap and adjust the physiochemical properties (Fig. 5c,d). The doping of Si^{4+} can induce a partial lattice distortion and an electronic effect that results in strain and atomic rearrangement, which can

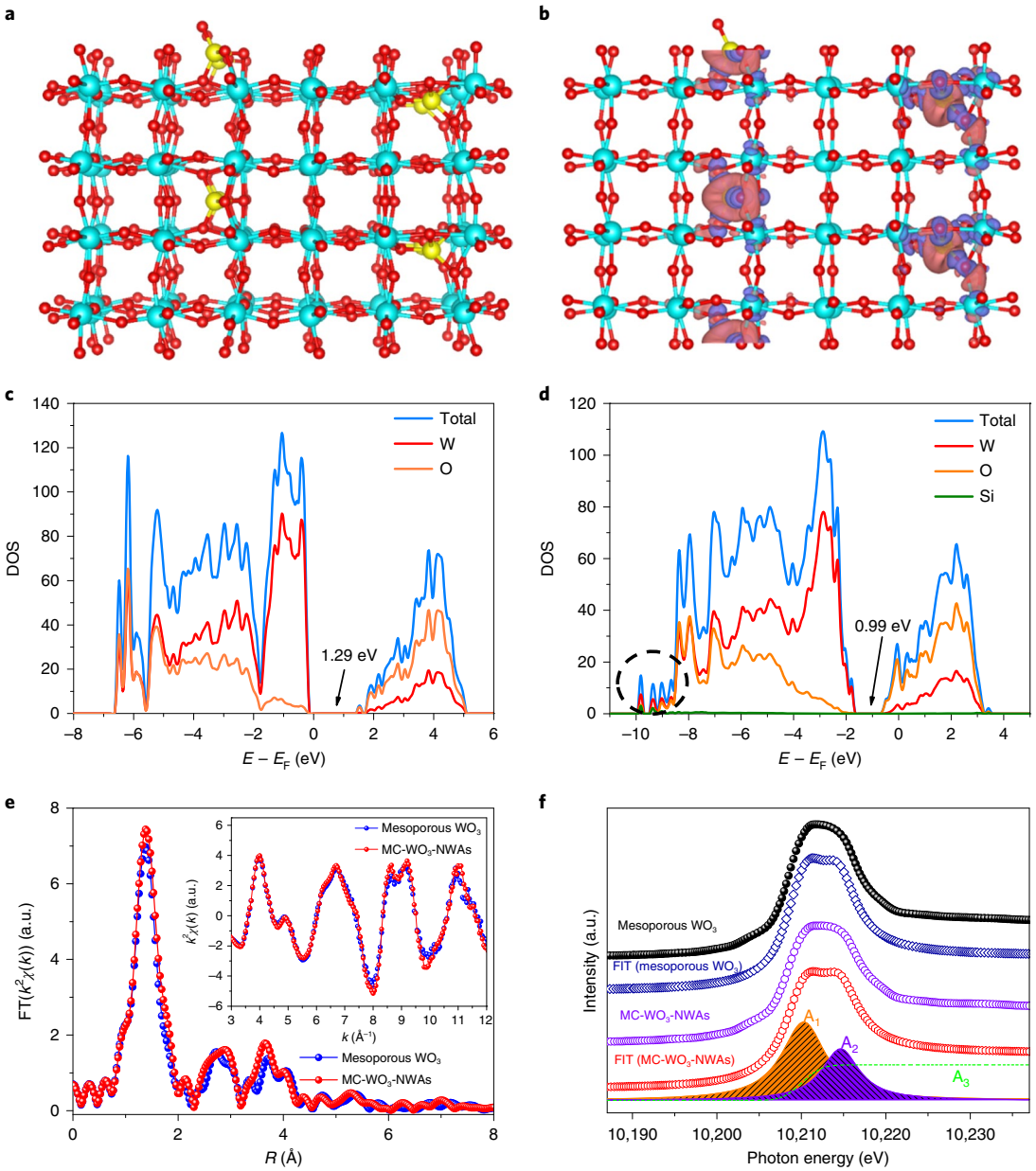

Fig. 5 | DFT calculation and EXAFS analysis of MC-WO_3-NWAs. a, The optimized structure of Si-doped WO_3. Red, oxygen atom; light blue, tungsten atom; yellow, silicon atom. **b**, Isosurface of a 3D electron density difference for the optimized Si-doped WO_3. **c**,**d**, Total and partial DOS of pure WO_3 (**c**) and Si-doped WO_3 (**d**). The dashed circle in **d** highlights the overlapping of the W, O and Si curves, implying strong hybridization. **e**, Fourier transform W L_3-edge EXAFS spectra of the samples. Inset: W L_3-edge EXAFS oscillation function $k^2\chi(k)$). **f**, W L_3-edge XANES spectra of Si-doped WO_3. The blue and brown isosurfaces represent charge accumulation and depletion, respectively, in the space. E_F, Fermi energy.

increase the conduction and electron transport capability. More computational details are shown in Supplementary Table 3 and Supplementary Note 5.

The local electronic and atomic structure of Si-doped ε-WO_3 were investigated by X-ray absorption near-edge spectroscopy (XANES) and extended X-ray absorption fine structure (EXAFS). W L_3-edge EXAFS spectra (Fig. 5e) were obtained via a Fourier transform treatment of the raw data (Supplementary Fig. 32). They show that Si-doped ε-WO_3 exhibits shifted peaks with higher intensities than those of pure WO_3, which demonstrates different local atomic arrangements (Supplementary Table 4 and Supplementary Note 6). The prominent resonance of XANES near the absorption edge in the energy region of 10,195–10,225 eV (Fig. 5f) is attributed to the excited electron transfer from W $2p_{3/2}$ to W 5*d* unoccupied states with multiple excitations for hybridized W 5*d*–O 2*p* conduction band states. The W L_3-edge spectra are consistent with the ε-WO_3 electronic structure based on crystal-field 10 D_q of the O_h symmetries. It exhibits two typical areas, A_1 and A_2, which correspond to the splitting of the W 5*d* orbital into the t_{2g} and e_g, respectively, degenerate states according to the crystal field effect[43]. By contrast, the decomposed $A_1(t_{2g})$ and $A_2(e_g)$ feature for Si-doped ε-WO_3 obtained from subtracting the arctangent (step function A_3) curve from the best fitted Gaussian curves (dashed green line in Fig. 5f) is different for pure WO_3. According to O_h crystal field theory, the introduction of Si^{4+} changes the t_{2g}–e_g splitting energy levels and DOS t_{2g} and e_g orbitals in the W 5*d*, which demonstrates a distortion of O_h symmetry due to the transformation from the γ-WO_3 to the ε-WO_3 phase by Si doping.

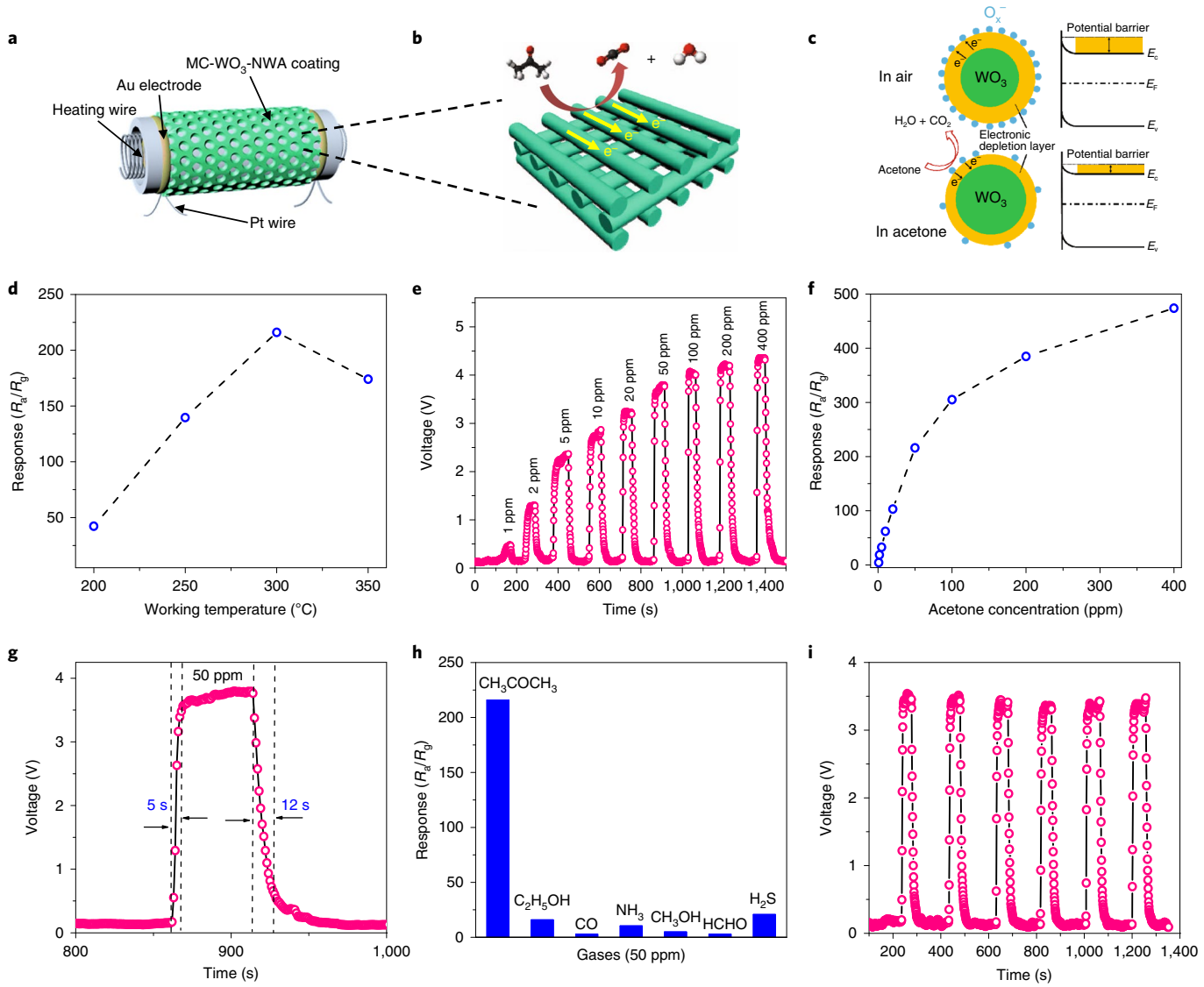

Fig. 6 | Gas-sensing performances of the MC-WO_3-NWAs. a, Sketch of the structure of a side-heated gas sensor on MC-WO_3-NWAs. **b**, Diagram of the interaction between acetone molecules and Si-doped ε-WO_3 nanowires. **c**, Schematic diagram of the mechanism for acetone-gas sensing. **d**, Response of the sensor to 50 ppm acetone at different temperatures. E_c, conduction band edge. E_v, valence band edge. **e**, Response–recovery curve of the sensor to acetone at different concentrations (1.0–400 ppm) at 300 °C. **f**, Response ($S = R_a/R_g$) of the sensor versus acetone concentrations. **g**, Response–recovery curve of the sensor to 50 ppm of acetone at 300 °C. **h**, Responses of the sensor to different 50 ppm gases at 300 °C (for example, S = 16 for 50 ppm ethanol and $S = 21$ for 50 ppm H_2S). **i**, Repeating response–recovery curve of the sensor to 50 ppm acetone.

Gas-sensing performances

The sensing performance of the MC-WO_3-NWAs was tested on a platform based on a side-heated type of gas sensor (Fig. 6a). The sensitivity is defined as $S = R_a/R_g$ for reducing gases (where R_a and R_g are the resistance of the sensor in air and tested gas, respectively) or $S = R_g/R_a$ for oxidizing gases, and the response of the sensor to the target gas can be calculated by detecting the changes in resistance (Supplementary Fig. 33). WO_3 is a typical n-type semiconductor, in which electrons behave as carriers. The oxygen molecules adsorbed on WO_3 could be activated as O_x^- species, such as O_2^-, O^- and O^{2-}, by extracting electrons from the conduction band of WO_3, which causes an increased resistance due to the formation of an electron depletion layer in the surface region of WO_3. When the sensor is exposed to reducing gases such as acetone, acetone molecules can react with the adsorbed oxygen species (acetone + O_x^- = CO_2 + H_2O + e^-), which releases the trapped electrons back to the conduction band. As a result, the sensor outputs a sensing signal of decreased resistance (Fig. 6b,c). In general, the activity of the sensing materials is strongly affected by working temperatures and even light illumination (Supplementary Figs. 33–35 and Supplementary Note 7)[44,45]. To optimize the working temperature, the WO_3-based sensor was tested towards 50 ppm of acetone at 200–350 °C (Fig. 6d). The sensing response first rises and then decreases with the increase of the testing temperature, and the sensitivity reaches its maximum at 300 °C. Thus, the working temperature was selected as 300 °C for subsequent tests.

The gas sensors show a fast response to various concentrations of acetone from 1.0 to 400 ppm (Fig. 6e) due to the highly open structure, abundant active sites and enhanced electron transport, and the resistance of the sensors can almost recover to their initial value, which indicates a good reversibility. Moreover, the response values (defined as $S = R_a/R_g$) continuously increase from 4.25 to 474 (Fig. 6f). The sensor in 50 ppm acetone displayed a response and recovery time of 5 and 12 seconds, respectively (Fig. 6g), indicative of

a fast response–recovery dynamics due to the highly open network of crossed nanowires that facilitates the diffusion of gas molecules. Compared to previously reported acetone sensors based on various WO_3 nanomaterials, our sensor shows an aggregate good sensing performance (Supplementary Table 5). Several works describe miniaturized gas sensors based on single nanowires of metal oxides that operate at room temperature, but suffer from various drawbacks, which include poor sensitivity and a long response–recovery time (Supplementary Table 6).

To study the selectivity of the sensor, six kinds of typical vaporous molecules, ethanol, carbon monoxide, ammonia, methanol, hydrogen sulfide and formaldehyde, were selected as the interfering gases. The response value of the sensor to 50 ppm acetone was 216, at least ten times higher than that of the six interfering gases under the same concentration (Fig. 6h). This indicates the good selectivity towards acetone of the sensor. Furthermore, the sensor displays a good cycling performance to 50 ppm acetone with a well-retained response (Fig. 6i), indicative of good stability. By contrast, the sensor based on mesoporous γ-WO_3 mentioned above exhibits similar response values towards ethanol (4.2) and acetone (5.7) without selectivity.

In summary, a general and flexible synthetic orthogonal assembly approach was developed to controllably construct 3D cross-stacked metal oxide nanowire arrays with well-interconnected frameworks and uniform nanowire spacings. Using the BCP-directed co-assembly approach with various commercial or synthetic Keggin-type POMs such as silicotungstic acid, silicomolybdic acid, phosphotungstic acid and phosphomolybdic acid, diverse multilayer-crossed nanowire arrays of doped metal oxide nanowire arrays with uniform nanowire thicknesses and spacings can be readily fabricated, such Si-doped WO_3, Si-doped MoO_3, P-doped WO_3 and P-doped MoO_3 for applications in resistors, biosensors, electrocatalysts and so on. The highly open and interconnected structure of the element-doped semiconducting nanowire arrays can provide a large amount of target–receptor interfaces and improved molecule diffusion, and a good charge transport, which makes them ideal candidates for various applications. As an example, the Si-doped ε-WO_3-based sensor shows acetone-sensing performances with a high sensitivity (a limit of detection of 10.0 ppb) and high selectivity to acetone, fast response/recovery dynamics and good stability. This study opens up a pathway to produce semiconductor nanowire arrays via a simple, general and scalable organic–inorganic co-assembly.

Online content

Any methods, additional references, Nature Research reporting summaries, source data, extended data, supplementary information, acknowledgements, peer review information; details of author contributions and competing interests; and statements of data and code availability are available at https://doi.org/10.1038/s41563-019-0542-x.

Received: 10 October 2018; Accepted: 23 October 2019;
Published online: 02 December 2019

References

1. Mao, L. B. et al. Synthetic nacre by predesigned matrix-directed mineralization. *Science* **354**, 107–110 (2016).
2. Ma, K. et al. Self-assembly of highly symmetrical, ultrasmall inorganic cages directed by surfactant micelles. *Nature* **558**, 577–580 (2018).
3. Prochowicz, D., Kornowicz, A. & Lewiński, J. Interactions of native cyclodextrins with metal ions and inorganic nanoparticles: fertile landscape for chemistry and materials science. *Chem. Rev.* **117**, 13461–13501 (2017).
4. Tan, K. W. et al. Transient laser heating induced hierarchical porous structures from block copolymer-directed self-assembly. *Science* **349**, 54–58 (2015).
5. Liu, X. G. et al. Complex silica composite nanomaterials templated with DNA origami. *Nature* **559**, 593–598 (2018).
6. Wang, F. D., Dong, A. G. & Buhro, W. E. Solution–liquid–solid synthesis, properties, and applications of one-dimensional colloidal semiconductor nanorods and nanowires. *Chem. Rev.* **116**, 10888–10933 (2016).
7. Dasgupta, N. P. et al. Semiconductor nanowires—synthesis, characterization, and applications. *Adv. Mater.* **26**, 2137–2184 (2014).
8. Yang, P. D. Wires on water. *Nature* **425**, 243–244 (2003).
9. Smith, P. A., Nordquist, C. D., Jackson, T. N. & Mayer, T. S. Electric-field assisted assembly and alignment of metallic nanowires. *Appl. Phys. Lett.* **77**, 1399–1401 (2000).
10. Chen, M. & Sun, L. Tuning the response of magnetic suspensions. *Appl. Phys. Lett.* **82**, 3310–3312 (2003).
11. Huang, Y., Duan, X. F., Wei, Q. Q. & Lieber, C. M. Directed assembly of one-dimensional nanostructures into functional networks. *Science* **291**, 630–633 (2001).
12. Law, W., Greene, L. E., Johnson, J. C., Saykally, R. & Yang, P. D. Nanowire dye-sensitized solar cells. *Nat. Mater.* **4**, 455–459 (2005).
13. Hochbaum, A. I. et al. Enhanced thermoelectric performance of rough silicon nanowires. *Nature* **451**, 163–168 (2008).
14. Kim, H. Monolithic InGaAs nanowire array lasers on silicon-on-insulator operating at room temperature. *Nano Lett.* **17**, 3465–3470 (2017).
15. Forster, S. & Dipl-Chem, T. P. From self-organizing polymers to nanohybrid and biomaterials. *Angew. Chem. Int. Ed.* **41**, 688–714 (2002).
16. Yang, J. K. W. et al. Complex self-assembled patterns using sparse commensurate templates with locally varying motifs. *Nat. Nanotechnol.* **5**, 256–260 (2010).
17. Doerk, G. S. et al. Enabling complex nanoscale pattern customization using directed self-assembly. *Nat. Commun.* **5**, 5805 (2014).
18. Bates, C. M. et al. Polarity-switching top coats enable orientation of sub-10-nm block copolymer domains. *Science* **338**, 775–779 (2012).
19. Amir Tavakkoli, K. G. et al. Multilayer block copolymer meshes by orthogonal self-assembly. *Nat. Commun.* **7**, 10518 (2016).
20. Wei, W. et al. Synthesis of molybdenum disulfide nanowire arrays using a block copolymer template. *Chem. Mater.* **28**, 4017–4023 (2016).
21. Jeong, J. W. et al. 3D cross-point plasmonic nanoarchitectures containing dense and regular hot spots for surface-enhanced Raman spectroscopy analysis. *Adv. Mater.* **28**, 8695–8704 (2016).
22. Zhao, D. Y. et al. Triblock copolymer syntheses of mesoporous silica with periodic 50 to 300 ångstrom pores. *Science* **279**, 548–552 (1998).
23. Lee, J. et al. Direct access to thermally stable and highly crystalline mesoporous transition-metal oxides with uniform pores. *Nat. Mater.* **7**, 222–228 (2008).
24. Thompson, R. B., Ginzburg, V. V., Matsen, M. W. & Balazs, A. C. Predicting the mesophases of copolymer–nanoparticle composites. *Science* **292**, 2469–2472 (2001).
25. Zhao, Y. et al. Small-molecule-directed nanoparticle assembly towards stimuli-responsive nanocomposites. *Nat. Mater.* **8**, 979–985 (2009).
26. Robbins, S. W. et al. Block copolymer self-assembly-directed synthesis of mesoporous gyroidal superconductors. *Sci. Adv.* **2**, 1501119 (2016).
27. Ferain, I., Colinge, C. A. & Colinge, J. P. Multigate transistors as the future of classical metal–oxide–semiconductor field-effect transistors. *Nature* **479**, 310–316 (2001).
28. Hochbaum, A. I. & Yang, P. D. Semiconductor nanowires for energy conversion. *Chem. Rev.* **110**, 527–546 (2010).
29. Hahm, J. & Lieber, C. M. Direct ultrasensitive electrical detection of DNA and DNA sequence variations using nanowire nanosensors. *Nano Lett.* **4**, 51–54 (2004).
30. Lunkenbein, T. et al. Direct synthesis of inverse hexagonally ordered diblock copolymer/polyoxometalate nanocomposite films. *J. Am. Chem. Soc.* **134**, 12685–12692 (2012).
31. Lunkenbein, T. et al. Access to ordered porous molybdenum oxycarbide/carbon nanocomposites. *Angew. Chem. Int. Ed.* **51**, 12892–12896 (2012).
32. Wu, Y. et al. Complexation of polyoxometalates with cyclodextrins. *J. Am. Chem. Soc.* **137**, 4111–4118 (2015).
33. Liu, S. H. et al. Patterning two-dimensional free-standing surfaces with mesoporous conducting polymers. *Nat. Commun.* **6**, 8817 (2015).
34. Wang, Z. M., Wang, W. D., Coombs, N., Soheilnia, N. & Ozin, G. A. Graphene oxide–periodic mesoporous silica sandwich nanocomposites with vertically oriented channels. *ACS Nano* **4**, 7437–7450 (2010).
35. Deng, Y. H. et al. Ordered mesoporous silicas and carbons with large accessible pores templated from amphiphilic diblock copolymer poly(ethylene oxide)-b-polystyrene. *J. Am. Chem. Soc.* **129**, 1690–1697 (2007).
36. Rydosz, A. et al. Performance of Si-doped WO_3 thin films for acetone sensing prepared by glancing angle d.c. magnetron sputtering. *IEEE Sens. J.* **16**, 1004–1012 (2016).
37. Wang, L., Teleki, A., Pratsinis, S. E. & Gouma, P. I. Ferroelectric WO_3 nanoparticles for acetone selective detection. *Chem. Mater.* **20**, 4794–4796 (2008).
38. Righettoni, M., Tricoli, A. & Pratsinis, S. E. Thermally stable, silica-doped ε-WO_3 for sensing of acetone in the human breath. *Chem. Mater.* **22**, 3152–3157 (2010).

39. Righettoni, M., Tricoli, A. & Pratsinis, S. E. Si:WO_3 sensors for highly selective detection of acetone for easy diagnosis of diabetes by breath analysis. *Anal. Chem.* **82**, 3581–3587 (2010).
40. Li, Y. H. et al. Highly ordered mesoporous tungsten oxides with a large pore size and crystalline framework for H_2S sensing. *Angew. Chem. Int. Ed.* **53**, 9035–9040 (2014).
41. Wang, C. et al. A shear stress regulated assembly route to silica nanotubes and their closely packed hollow mesostructures. *Angew. Chem. Int. Ed.* **52**, 11603–11606 (2013).
42. Luo, W. et al. A Resol-assisted co-assembly approach to crystalline mesoporous niobia spheres for electrochemical biosensing. *Angew. Chem. Int. Ed.* **52**, 10505–10510 (2013).
43. Wang, Y. C. et al. Structural distortion and electronic states of Rb doped WO_3 by X-ray absorption spectroscopy. *RSC Adv.* **6**, 107871–107877 (2016).
44. Comini, E., Cristalli, A., Faglia, G. & Sberveglieri, G. Light enhanced gas sensing properties of indium oxide and tin oxide sensors. *Sens. Actuators B* **65**, 260–263 (2000).
45. Zhang, H., Qin, H. W., Gao, C. Y. & Hu, J. F. An ultrahigh sensitivity acetone sensor enhanced by light illumination. *Sensors* **18**, 2318 (2018).

Methods

Synthesis of multilayer-crossed nanowire arrays of Si-doped WO_3. A typical synthesis was carried out as follows: 0.10 g of the amphiphilic diblock copolymer PEO_{114}-b-PS_{156} (M_n = 21,500 g mol^{-1}, polydispersity index = 1.06) designed through a classical atom-transfer radical polymerization strategy[40] was dissolved in 4.0 ml of THF with a high-speed mixer to form a homogeneous solution. Almost simultaneously, 0.30 g of H_4SiW (analytical reagent grade (AR), Aladdin) was also dissolved in 1.0 ml of THF to form the precursor solution. After all the solid-phase components had been dissolved, they were mixed to produce a light-blue colloidal solution (the mass ratio of PEO-b-PS/POMs was 1:3). After 1.0 h, this solution was cast onto glass Petri dishes to evaporate THF slowly at room temperature for 12 h (air humidity 20–60%), followed by a sequential thermal treatment at 50 °C and 100 °C for 24 h each. The target Si-doped WO_3 film was generated through a gradient calcination treatment at 500 °C for 1 h in N_2 (heating rate, 1 °C min^{-1} below 350 °C and 5 °C min^{-1} above 350 °C) and then at 400 °C for 20 min in air (5 °C min^{-1}).

Synthesis of multilayer-crossed nanowire arrays of P-doped WO_3. MC-P-WO_3-NWAs were synthesized by following the same method as that for the multilayer-crossed nanowire arrays of Si-doped WO_3 except that commercial phosphotungstic acid hydrate ($H_3PW_{12}O_{40}$·21H_2O, AR, Sigma-Aldrich) was used as the inorganic precursor.

Synthesis of multilayer-crossed nanowire arrays of Si-doped MoO_3 and P-doped MoO_3. The MC-Si-MoO_3-NWAs and MC-P-MoO_3-NWAs were synthesized by following a similar method except that commercial silicomolybdic acid hydrate ($H_4SiMo_{12}O_{40}$·30H_2O, AR, Aladdin) and phosphomolybdic acid hydrate ($H_3PMo_{12}O_{40}$·30H_2O, AR, Aladdin) were used as inorganic precursors, respectively. The mass ratio of PEO-b-PS/POMs was 1:2. The thermal treatment procedure was calcination at 350 °C for 2 h in a N_2 atmosphere (1 °C min^{-1}) and 400 °C for 30 min in air (5 °C min^{-1}).

Synthesis of MC-WO_3-NWAs using PB_{18k}-b-PEO_{7k} as the structure-directing agent. The synthesis follows the same procedure as that for MC-WO_3-NWAs except that PB_{18k}-b-PEO_{7k} diblock copolymers were used as the structure-directing agent to co-assemble with inorganic H_4SiW. Using the optimal mass ratio of PB_{13k}-b-PEO_{7k}/H_4SiW of 1:4.5, multilayer-crossed Si-doped WO_3 nanowire arrays were readily obtained (Supplementary Fig. 22).

Characterizations and measurements. The scanning electron microscopy images were collected with a Zeiss Ultra 55 FESEM recorded at 3 kV. The dried samples were directly used for observation without any treatment. The TEM images were recorded with a JEM-2100 F (JEOL) microscope. The N_2-adsorption isotherms were obtained at 77 K with a Micromeritics Tristar 3020 analyser. To remove impurities (such as adsorbed H_2O), all the target materials were degassed in vacuum conditions (180 °C, 6 h) and, in addition, the specific surface area was recorded with a Brunauer–Emmett–Teller technique and the pore size distribution was measured via a Barrett–Joyner–Halenda strategy. Fourier transform infrared spectra of all the samples were obtained with classical KBr pellets with a Nicolet Fourier spectrophotometer. Thermogravimetric analysis data were collected from 25 to 800 °C in air (SDTQ600 analyser, heating rate 10 °C min^{-1}). The in situ TEM tests were carried out in a differentially pumped Hitachi H-9500 ETEM operating at 300 keV with a home-made microelectromechanical-system-based ultrastable heating holder[46]. The ETEM was evacuated to a base vacuum of 10^{-4} Pa. The heating process was performed in vacuum (<10^{-4} Pa) using the heating stage with a constant heating rate (40 °C min^{-1}).

Gas-sensing tests. The gas sensing performances of all the samples were evaluated on a typical side-heated type of gas sensor by a sensing system (HW-30A, Hanwei Electronics Co. Ltd). To quantitatively evaluate the material properties, the response value is considered as S was used. Moreover, the response time and recovery time are the times to achieve a 90% saturation value after the import and/or release of the target gas within the step function. For all the tests, the MC-WO_3-NWA powder was dispersed into terpineol to produce a uniform paste. The as-prepared slurry samples were deposited on an alumina tube for 2 h of annealing at 100 °C and further solidifying at 300 °C for 2 h. The coating on each single ceramic tube contained 5.0 ± 0.5 mg WO_3 nanowire materials. The distance between the two Au electrodes was 2.0 mm on average. The thickness of the coating was 500 µm on average. The electric resistance of the sensor device under ambient atmosphere was about 11 ± 3 MΩ at the optimum working temperature (300 °C) and an illustration of the electric circuit of a sample is shown in Supplementary Fig. 33.

DFT theoretical calculations. DFT calculations were used to evaluate the structural relaxation and electronic properties of MC-WO_3-NWAs, and our calculations on the WO_3 complex were performed using the plane-wave basis Vienna Ab-initio Simulation Package code[47,48] and the projector augmented wave method used to describe the electron–ion interaction[49–51]. The exchange-correlation functional of the generalized gradient approximation[52,53] was applied to describe the exchange correlation potential. For geometry optimization, the Brillouin zone was sampled with a Monkhorst–Pack mesh[54] of 5 × 5 × 2 k-points. The cutoff energies for the plane waves were set to be 400 eV, and the convergence tolerance of force on each atom during the structure relaxation was set at 0.02 eV Å^{-1}. The self-consistent field iterations were considered converged when the change of total energy was smaller than 10^{-5} eV. The room-temperature monoclinic structure for the pristine γ-WO_3 model with a typical space group $P21/n$ was constructed based on the structure of an octahedron and the optimized unit cell parameters were a = 7.294 Å, b = 7.418 Å, c = 7.591 Å and β = 91.5°, and the optimized unit cell consisted of 8 W and 24 O atoms. The formation energy (E_{form}) of the doping system was calculated as $E_{form} = E_{WO_3} - E_{WO_3\text{-}Si} + \mu_{Si}$, where $E_{WO_3\text{-}Si}$ is the total energy of the WO_3–Si system, E_{WO_3} is the total energy of pure WO_3 and μ_{Si} is the chemical potential of Si. The results are listed in Supplementary Table 4.

XAFS measurements and analysis. To explore the local structural and compositional environment of the absorbing atom, the W L_{III}-edge XAFS spectra for pure WO_3 and Si-doped ε-WO_3 were obtained from the Shanghai Synchrotron Radiation Facility. During the data-collection process, all the data were recorded with a typical fluorescence mode based on a high-purity Ge solid-state detector, and all the signals given are average values of triplicates. To obtain structural information, all the spectra were collected through a classical fitting via the common IFEFFIT software[55,56]. In addition, the theoretical EXAFS amplitudes, including phase functions for W–O single-scattering paths, were generated based on FEFF 7.0[43,57]. The main fitted parameters, such as interatomic distance, coordination number and Debye–Waller factor were also confirmed with reasonable guesses and were fitted in R-space[43].

Data availability

The datasets generated and/or analysed during the current study are available from the corresponding author on reasonable request.

References

46. Li, M. et al. Effect of hydrogen on the integrity of aluminium-oxide interface at elevated temperatures. *Nat. Commun.* **8**, 14564 (2017).
47. Kresse, G. & Furthmüller, J. Efficiency of ab-initio total energy calculations for metals and semiconductors using a plane-wave basis set. *Comput. Mater. Sci.* **6**, 15–50 (1996).
48. Kresse, G. & Furthmüller, J. Efficient iterative schemes for ab initio total-energy calculations using a plane-wave basis set. *Phys. Rev. B* **54**, 11169–11186 (1996).
49. Blöchl, P. E. Projector augmented-wave method. *Phys. Rev. B* **50**, 17953–17979 (1994).
50. Kresse, G. & Joubert, D. From ultrasoft pseudopotentials to the projector augmented-wave method. *Phys. Rev. B* **59**, 1758–1775 (1999).
51. Methfessel, M. & Paxton, A. T. High-precision sampling for Brillouin-zone integration in metals. *Phys. Rev. B* **40**, 3616–3621 (1989).
52. Perdew, J. P., Burke, K. & Ernzerhof, M. Generalized gradient approximation made simple. *Phys. Rev. Lett.* **77**, 3865–3868 (1996).
53. Perdew, J. P. & Wang, Y. Accurate and simple analytic representation of the electron-gas correlation energy. *Phys. Rev. B* **45**, 13244–13249 (1992).
54. Monkhorst, H. J. & Pack, J. D. Special points for Brillouin-zone integrations. *Phys. Rev. B* **13**, 5188–5192 (1976).
55. Webb, S. M. SIXpack: a graphical user interface for XAS analysis using IFEFFIT. *Phys. Scr.* **T115**, 1011–1014 (2005).
56. Newville, M. J. IFEFFIT: interactive XAFS analysis and FEFF fitting. *J. Synchrotron Rad.* **8**, 324–332 (2001).
57. Rehr, J. J., Albers, R. C. & Zabinsky, S. I. High-order multiple-scattering calculations of X-ray-absorption fine structure. *Phys. Rev. Lett.* **69**, 3397–3400 (1992).

Acknowledgements

This work was financially supported by the National Natural Science Foundation of China (Grant nos 51422202, 21673048 and 21875044), Key Basic Research Program of Science and Technology Commission of Shanghai Municipality (17JC1400100) and Youth Top-notch Talent Support Program of China. The authors thank G. Zhou and Z. Shan for assistance in TEM characterization.

Author contributions

Y.R., Y.Z. and Y.D. conceived the project and designed the experiments. Y.R., Y.Z., X.Z., J.M., D.Z., G.W. and Y.D. were primarily responsible for the data collection and analysis. Y.L. and Y.A. analysed the structures with DFT calculations. S.X. and Y.Z. analysed the EXAFS data. Y.R., Y.Z. and Y.D. prepared the figures and wrote the main manuscript text. All the authors contributed to the discussions and manuscript preparation.

Competing interests

The authors declare no competing interests.

Additional information

Supplementary information is available for this paper at https://doi.org/10.1038/s41563-019-0542-x.

Correspondence and requests for materials should be addressed to Y.D.

Reprints and permissions information is available at www.nature.com/reprints.